Model for the robust mechanical behavior of nacre

A.G. Evans and Z. Suo
*Department of Mechanical and Aerospace Engineering and Princeton Materials Institute, Princeton
University, Princeton, New Jersey 08544*

R.Z. Wang and I.A. Aksay
*Department of Chemical Engineering and Princeton Materials Institute, Princeton University,
Princeton, New Jersey 08544*

M.Y. He
Materials Department, University of California, Santa Barbara, California 93106

J.W. Hutchinson
Division of Engineering and Applied Science, Harvard University, Cambridge, Massachusetts 02138

The inelastic deformation of nacre that leads to its structural robustness has been characterized in a recent experimental study. This article develops a model for the inelastic behavior, measured in tension, along the axis of the aragonite plates. The model is based on observations for abalone nacre that the inelasticity is associated with periodic dilatation bands. These bands contain coordinated separations at the periphery of the plates. The separations open as the material strains. The response is attributed to nanoscale asperities on the surfaces of the plates. The model calculates the stresses needed to displace the plates, resisted by elastic contacts at the asperities. The results are compared with the measured stress/strain curves.

I. INTRODUCTION

Various naturally occurring materials have inherent mechanical robustness, despite the brittle nature of their predominant constituent: $CaCO_3$, often present as aragonite.[1–7] This robustness is manifest in inelastic strains prior to rupture.[1,8] An example is presented on Fig. 1, for nacre, which consists of high aspect ratio aragonite plates separated by a very thin polymer interlayer.[9,10] Its inelastic response is anisotropic, being dependent upon the loading and its orientation relative to the coordinates of the aragonite plates.[8] Upon loading in tension parallel to the plates, the material "yields" after an initial elastic response (Young's modulus, $E = 70$ GPa), exhibits rapid strain hardening, and, thereafter, deforms subject to a steady-state stress, $\sigma_{ss} \approx 110$ MPa (minimal strain hardening) up to a strain of about 1% [Fig. 1(a)].[8] Unloading and reloading indicates a permanent strain and hysteresis [Fig. 1(b)].[1] In compression, the material remains elastic and fails at a strain exceeding 0.5% [Fig. 1(a)].[8] Loading at $\pi/4$ to the plates, to induce a uniform shear across the interfaces, elicits another inelastic response, exhibiting strains in excess of 8%,[8] subject to a shear resistance, $\tau_{ss} \approx 40$ MPa [Fig. 1(c)].

The consequence of inelasticity, particularly that in tension, is an insensitivity to severe strain concentration sites, because the inelastic deformation reduces (and in some cases, eliminates) stress concentrations.[11–14] Such an inelastic zone has been observed for nacre.[8] While there are precedents for mechanically robust materials made from predominantly brittle, oxide, constituents,[12,14] the enabling topologies found in nacre are unique. Namely, robustness is realized in a brittle, tabular phase ($CaCO_3$) by dispersing a minimal amount (<5%) of polymer. The primary role of the polymer is to impart transverse integrity across the plates, because of its strong adhesion to the aragonite and its remarkable capacity for inelastic stretch.[6] It also appears to lubricate the interfaces.

Upon loading in tension along the plate axis, the inelastic behavior coincides with the formation of "dilatation" bands, which are visible because of deformation-induced optical scattering centers (Fig. 2).[2,8] While these bands differ in detail between columnar and sheet nacre, there appear to be three common characteristics: (i) They form normal to the applied load once the elastic limit has been exceeded. The number density of the bands increases as the stress increases, until saturation is reached. (ii) They are visible because microscale separations form at the perimeter of each of the plates, which act as scattering sites. The inelastic strain derives from the opening displacements at these separations, accumulated over all of the bands located within the gauge section. (iii) The growth of the separations (and hence the inelastic strain) is enabled by slip occurring at
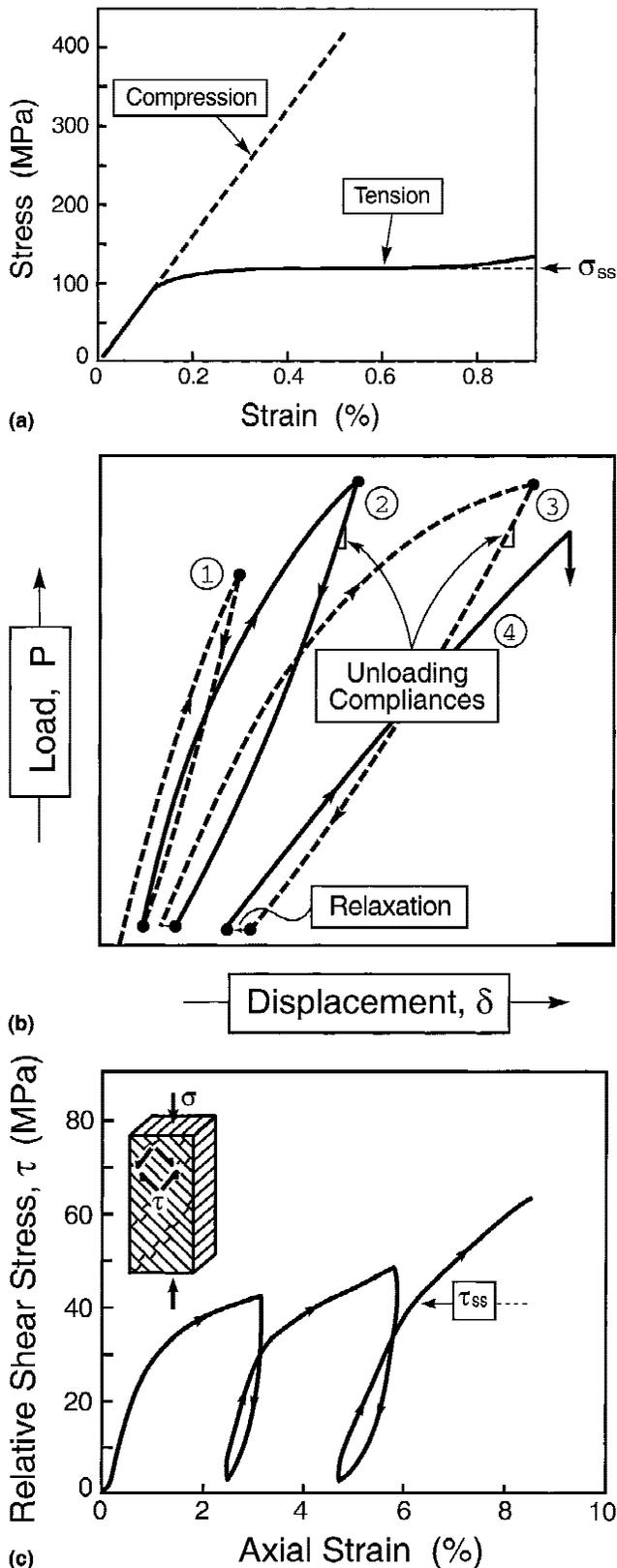
FIG. 1. Stress/strain characteristics of nacre: (a) stress/strain curves in tension and compression measured along the plate axis;[8] (b) several consecutive load/unload curves highlighting the hysteresis;[1] (c) shear stress/strain response for slip along the plate interfaces.[8]

the adjoining plate interfaces. The slip resistance is provided by nanoscale asperities on the plate surfaces. In the saturated state, all plates exhibit peripheral separations.

The inelastic deformation involves the slip of $CaCO_3$ nano-asperities against each other, accompanied by the deformation of the intervening polymer. The flow resistance beyond the elastic limit is related to the associated shearing, given a representation compatible with the tensile and shear stress/strain curves [Figs. 1(a)–1(c)]. The approach taken is to simulate the slip process by taking into account all of the known physical properties of the $CaCO_3$ plates, including their dimensions, as well as the topologies of the nano-asperities. The role of the polymer is implicit, through its effect on ensuring the integrity of the plates[6] and its influence on the friction occurring at the contacting asperities. Its possible role in resisting plate shear cannot be incorporated in the model, since its constitutive behavior is unknown. Its neglect in the model is justified by the comparison between the simulated and measured stress/strain curves.

The process to be described has close similarities with the behavior of fibrous oxides that acquire their inelastic strain capacity from thin interface layers susceptible to debonding and frictional slip, enabled by the occurrence of matrix cracks[12–14] (Appendix I). Related effects occur in thin brittle films on ductile substrates,[15–18] which crack in a periodic manner with associated inelastic strain. However, in such cases, there are no frictional effects at the interfaces. Instead, the inelastic strain derives from the elastic opening of the cracks and the plastic strains in the substrate between the cracks.

II. UNDERLYING MECHANISMS

A. Mechanistic basis

The deformation has a preliminary linear elastic stage. This stage arises since the polymer interlayer at the edges of the plates, as well as a small number of intact aragonite bridges across the plates, are able to sustain the load, until they rupture. Subsequently, an inelastic shearing process occurs, resisted by the nano-asperities on the surfaces of the aragonite plates (Figs. 3 and 4). The asperities are topographically matched prior to loading but, otherwise, have dispersed wavelengths and aspect ratios.[8] The inelastic shear process is considered to occur in two stages (Figs. 3 and 4): (i) The matched asperities climb over each other until they juxtapose. (ii) The plates slip over the asperity peaks in "steady-state." The analysis assumes plane strain conditions.

Two basic mechanics concepts are crucial to the model: (i) When the first separations nucleate, at the elastic limit, the shear resistance of the plate interfaces must be low enough to assure that a dilatation band forms rather than a brittle crack.[19] (ii) Thereafter, large-scale inelastic deformation is incontrovertibly linked to strain
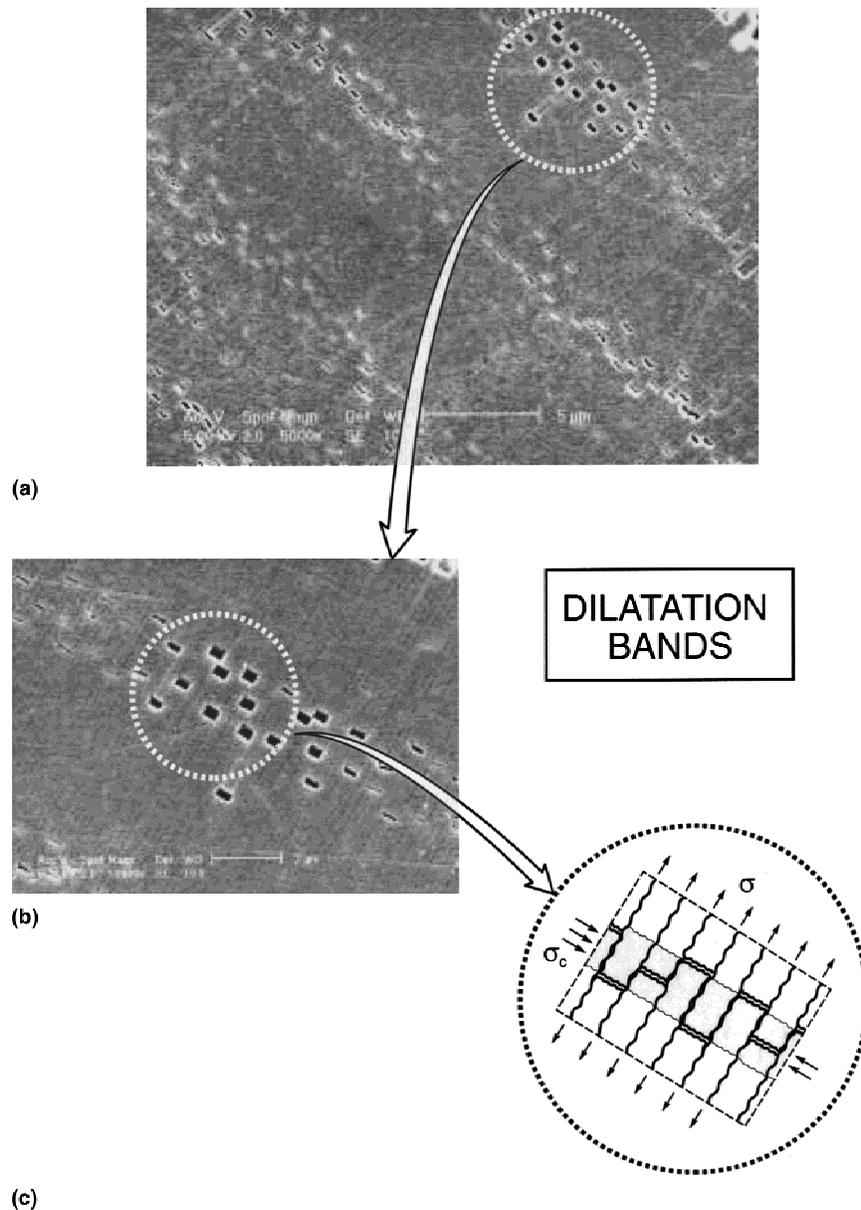
FIG. 2. Scanning electron microscope images of the dilatation bands found in nacre upon tensile straining along the plate axis. Note the asperities on the plate interfaces that resist slip.

hardening. Namely, in the absence of hardening, all of the inelastic deformation would localize in the first band, failure would be catastrophic at the nucleation stress,[20,21] and the material would be brittle. Conversely, when the stress needed to continue straining increases with deformation, the stress elsewhere also increases and seeks new bands. With sufficient hardening, all possible sites can be activated, resulting in the maximum inelastic strain allowed by the mechanism, ensuring a robust, ductile response. Such hardening is attributed, below, to the asperities (Figs. 3 and 4).

Asperity climb is addressed by solving the slip problem in the presence of a matching, periodic array of asperities on opposing plates (Fig. 4). Analysis of

"steady state" requires a slipping friction solution for a pair of plates with periodic asperities. Both stages are addressed. The models are developed in detail for abalone nacre, because the tessellated morphology of the plates and the consequent discreteness of the dilatation bands (Fig. 2) allows a representative unit cell to be defined and analyzed numerically (Figs. 4 and 5). The stochastics governing the inelastic response of sheet nacre[8] are assessed at a more qualitative level.

B. Asperity climb

For asperities to translate past each other within a deformation band, the material in the band must dilate, laterally. This dilatation is constrained by the nonslipping
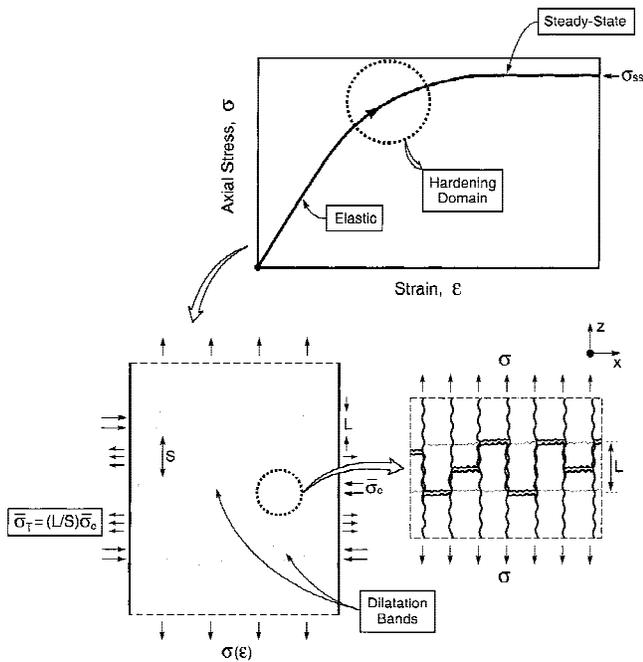
FIG. 3. Schematic diagram of several dilatation bands indicating the transverse compressions in the band and the compensating tensions between the bands.

material outside the deformation band, causing the development of a transverse internal compression and a compensating tension outside (Fig. 3). The induced compression is the source of strain hardening. It increases as the asperities translate, thereby elevating the axial force required for additional slip. The magnitudes of these stresses and their effect on slip are calculated below for typical plate dimensions and asperity morphologies.

The situation envisaged for each band has been illustrated schematically on Fig. 3. That is, as the bands widen and the separations open, all of the axial interfaces within the band experience slip, with an explicit shear resistance, designated τ. This shear resistance increases as the opening of the separations, u, increases, causing the associated axial stress, σ, to increase, resulting in hardening. All other interfaces are considered static (nonslipping). The unit cell characterizing this process is shown on Fig. 4(a). The asperities are considered to be sinusoidal, with fixed wavelength and amplitude. The associated stress/displacement behavior is depicted schematically on Fig. 4(c). Once the contacting asperities juxtapose, the stress required for this process to continue attains a "steady-state" σ_{ss}, as the compressed asperities slip over each other, along their peaks. The asperity climb model is discontinued at juxtaposition.

The slipping interfaces are modeled using conventional friction concepts, in the sense that the contacts are assigned a Coulomb friction coefficient, μ. This choice allows the modeling to proceed in a manner that brings

out many of the key ideas. (However, any friction law that allows τ to increase as the displacement proceeds would yield the same general result.) The intent of the calculations is to determine the axial stress, σ, as a function of the opening of the separations, u, and to establish the influence of the key variables on $\sigma(u)$ up to and including the onset of "steady state." The stress/strain response is determined directly from $\sigma(u)$ upon noting that the inelastic strain, ϵ_p, is related to the opening displacement by:

$$\epsilon_p = u/S \quad , \tag{1}$$

where S is the spacing between the dilatation bands. To establish the scope of the numerical calculations, and to identify the salient nondimensional parameters, an analytical approximation has been derived (see Appendix II).

The model also gives the transverse compressive stresses within the bands, average $\overline{\sigma}_c$, and the balancing tension $\overline{\sigma}_T$ between the bands, which are related by

$$\overline{\sigma}_T = \overline{\sigma}_c L/S \quad , \tag{2}$$

where L is the band thickness. The former governs the strain hardening, while the latter establishes a criterion for integrity of the plates.

C. Steady-state slip

While the shear resistance of plates with periodic asperities on their surfaces can be calculated numerically, subject to Coulomb friction,[22,23] such analysis is nontrivial and beyond the scope of this article. The alternative is to use the slip resistance.[8] These authors conducted compression tests on specimens with the plate interfaces at 45° to the load axis [Fig. 1(c)]. By resolution of the stress along the slip planes, the shear resistance is $\tau_{ss} \approx 40$ MPa, subject to a transverse compression, $\sigma_c \approx 40$ MPa. This shear stress is used in the subsequent interpretation of the tensile stress/strain curve.

III. HARDENING MODEL

A. Tensile strains

The finite element method has been used for numerical analysis of the tensile stress/strain response. In all of the calculations (Fig. 4), the wavelength of the asperities, $2l$, and their amplitude, A, are taken to be small relative to the band thickness, L, consistent with the observations.[8] The aragonite plate width is D, and ν is Poisson's ratio. The results have been obtained using the ABAQUS code, which contains an option for solving contact problems with friction, using the properties $E = 70$ GPa and $\nu \approx 0.2$. The mesh is shown in the deformed state (Fig. 5), to emphasize the contact zone between asperities. Note that a very fine mesh has been used to give an accurate
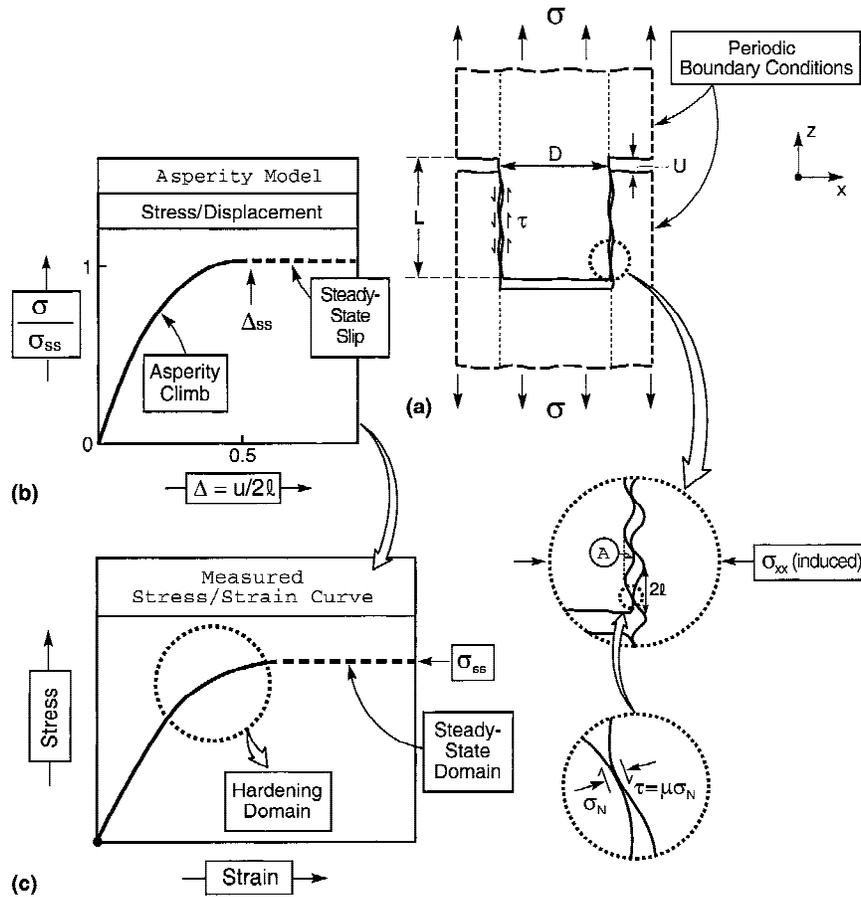
FIG. 4. Unit cell used for analysis of the pull-out stress/displacement relation for the nano-asperity model. The expected stress/displacement behavior and the consequent stress/strain curve are sketched as insets, as well as the asperity slip model.

accounting of the contact. The displacement is normalized using $\Delta = u/2l$. Insights from Appendix II suggest a stress normalization, $\Gamma \equiv [\sigma D^2/EAL][1 + \nu L/D]$, as plotted on Fig. 6. Note that there is a finite stress even when the friction coefficient is zero. The trends at $\mu = 0$ are plotted on Fig. 7. In this case, the stress normalization $\Sigma \equiv \Gamma(L/D)$ provides a rationalization, for the reasons elaborated below.

Upon inspection, the behavior obtained within the range ($0 \leq \mu \leq 0.3 : 1 \leq L/D \leq 8$) can be represented by the approximate expression:

$$\Gamma \equiv \frac{\sigma D^2}{EAL}(1 + \nu L/D)$$
$$\approx \left[\mu \sin(\pi\Delta) + c_\mu \frac{D}{L}\sin(2\pi\Delta)\right] \quad, \tag{3}$$

where

$$c_\mu = 0.147 - 0.375\mu + 0.422\mu^2 \quad.$$

The first term represents the frictional contribution to the slip resistance [$\mu\sigma_N$ in Fig. 4(d)], while the second term

is the contribution from the normal traction [σ_N in Fig. 4(d)]. The curves obtained using Eq. (3) are compared with some of the numerical results on Fig. 6.

Corresponding expressions for the stress and the displacement at the peak are found by differentiating Eq. (3). Upon letting $\chi = \pi u/2l$,

$$\Gamma = \mu \sin\chi + c_\mu \frac{D}{L}\sin(2\chi) \quad, \tag{4a}$$

such that, on differentiation

$$\frac{\partial\Gamma}{\partial\chi} = \mu\cos\chi + c_\mu \frac{2D}{L}\cos(2\chi) \quad. \tag{4b}$$

At the maximum, $\partial\Gamma/\partial\chi = 0$:

$$2\cos^2\chi + \frac{\mu L}{2Dc_\mu}\cos\chi - 1 = 0 \quad. \tag{4c}$$

At the stress maximum, where $\chi \equiv \chi^{ss}$,

$$\cos(\chi^{ss}) = 0.25\left[\sqrt{\left(\frac{\mu L}{2Dc_\mu}\right)^2 + 8} - \frac{\mu L}{2Dc_\mu}\right] \quad. \tag{4d}$$
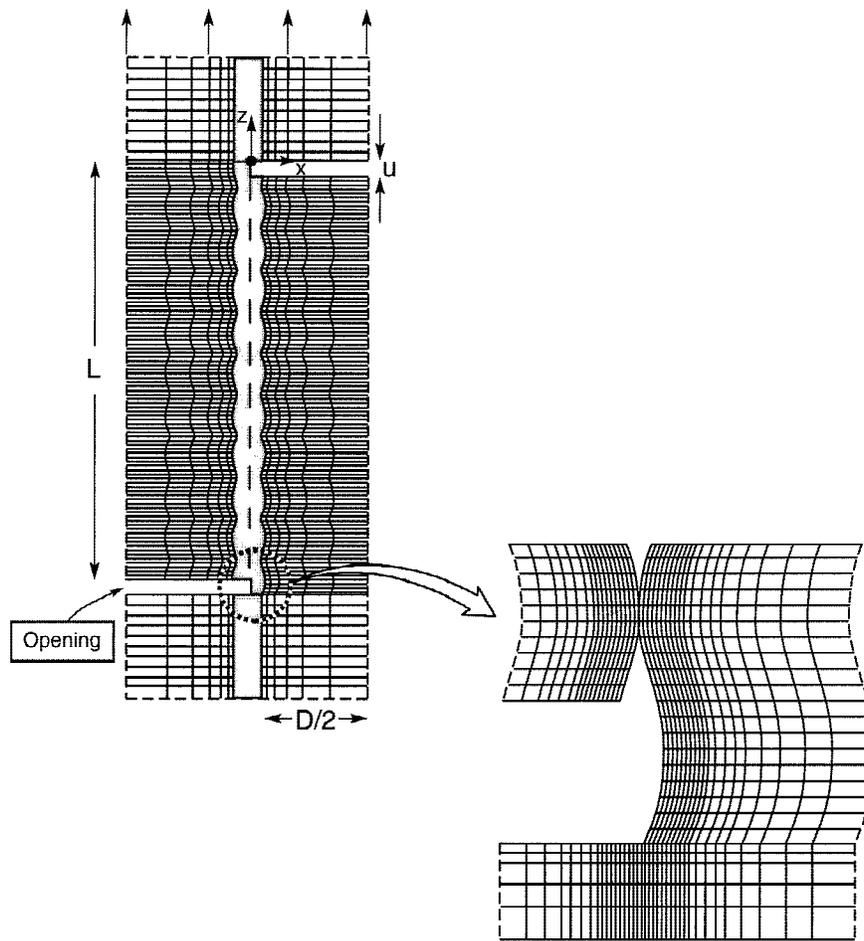
FIG. 5. Finite element mesh used for the numerical analysis, shown at a displacement where the asperities are elastically compressed.

The results, plotted on Fig. 8, are used below to compare the predictions with the measured stress/strain curves.

B. Transverse stresses and strains

Illustrative results for the lateral stresses created within the plates, as the bands dilate, are plotted on Fig. 9(a). The lateral *compressive stresses* within the dilatation bands are nonuniform, because of the Poisson effect. That is, near the separations, where the axial stresses are zero, there is no Poisson contraction and the compressions are large. Conversely, near the edge of the bands, the Poisson contraction causes a transverse compressive stress (see Appendix II).

The lateral *tensile* stresses between the bands are given approximately by [Appendix II: Eq. (B2)]:

$$\overline{\sigma}_c \approx \sigma_{ss} \sin[\pi\Delta] - \nu\sigma \quad .$$

At the interfaces just outside the bands, there is a stress concentration [Fig. 9(b)]. The stresses are singular but diminish to an essentially uniform level at a small distance from the band, $z/D \approx -0.1$. It is suggested that one role of the organic interlayer is to sustain such large strains through its large inelastic tensile stretch.[6]

IV. COMPARISON WITH MEASUREMENTS

A. Stress/strain curve

A comparison between the model and the measurements is made at two levels: (i) In the hardening domain, the stress/strain response is predicted from Eq. (3) with Eq. (1), by inputting measured dimensional parameters[8] ($D = 0.5$ μm, $L = 1.5$ μm, $A = 8$ nm, $2l = 50$ nm, and $S = 8$ μm, with $E = 70$ GPa and $\nu \approx 0.2$), as well as the stress maximum obtained from Eq. (4). A comparison is made with the measured curve (Fig. 7): nondimensional stress maximum, $\Sigma_{ss} = 0.14$, and corresponding displacement, $\Delta_{ss} = 0.2$. For a friction coefficient, $\mu = 0$, the stress maximum is $\sigma_{ss} \approx 98$ MPa, compared with a measured strength $\sigma_{ss} \approx 110$ MPa [Fig. 1(a)]. Exact coincidence is achieved when $\mu \approx 0.02$. The inference is that the interface is essentially *frictionless*. The corresponding opening displacement, used with Eq. (1), indicates an inelastic strain at steady state, $\epsilon_p \approx 0.16\%$. This adds to an elastic strain, $\epsilon_{el} \equiv \sigma_{ss}/E \approx 0.12\%$, resulting in a total strain, about 0.28%, consistent with the strain measured at the beginning of the stress plateau [Fig. 1(a)]. (ii) The independently measured slip resistance

tance, τ_{ss} (Sec. II. C), is used to evaluate σ_{ss} by implementing Eq. (B4) from Appendix II: $\sigma_{ss} = \tau_{ss}[L - u]/D$, in the limit $u \ll L$. This assessment gives a stress, $\sigma_{ss} \approx$ 120 MPa, which is also similar to the measured value.

Both approaches thus appear to yield a consistent description of the stress/strain response in terms of the slip of the plate interfaces, resisted by nano-asperities. The role of the polymer is surmised to be in providing frictionless asperity contacts.

B. Transverse stresses

The average lateral compression induced in the bands at the steady-state stress is obtained from (Fig. 9) as $\bar{\sigma}_c \approx$ 200 MPa. This is appreciably higher than the transverse stress in the compression test [$\sigma_c \approx$ 40 MPa, Fig. 1(c)]. The corresponding transverse tension between the bands
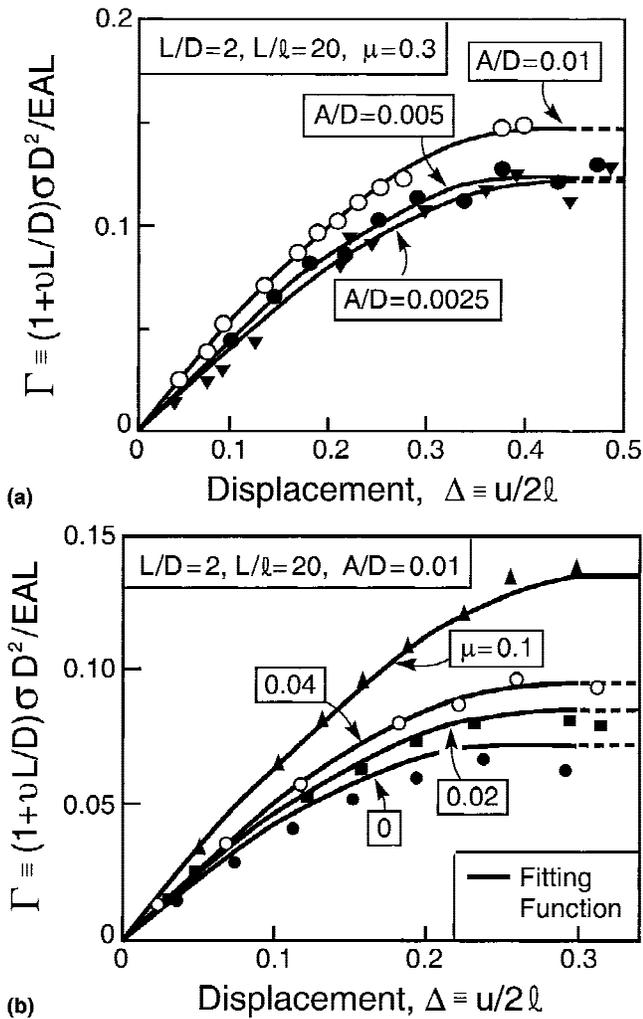
is $\bar{\sigma}_T \approx$ 65 MPa. It is proposed that one major role of the organic interlayer is to sustain this transverse stress, enabled by its appreciable capacity for plastic stretch.[6] Accordingly, the organic appears to have three functions. That situated along the transverse plates must have
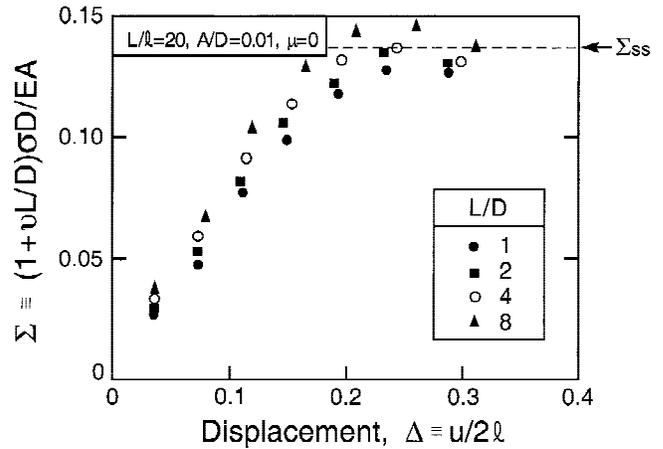

FIG. 7. Effect of the pull-out length L/D on the stresses at zero friction.

FIG. 6. Calculated stress/displacement results: (a) effect of the asperity amplitude, A/D, for a friction coefficient, $\mu = 0.3$; (b) influence of the fiction coefficient. On the latter, note that the stress is finite even when $\mu = 0$. The stresses and displacements have been nondimensionalized as elaborated in the text.
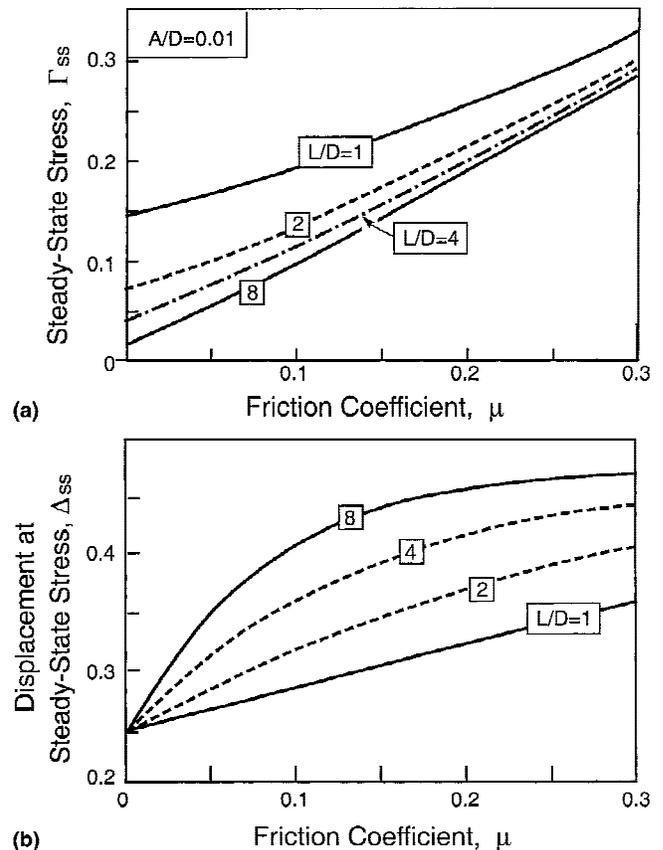

FIG. 8. Variations in (a) the steady-state stress and (b) the displacement at the onset at steady state, as a function of the friction coefficient for various pull-out lengths, L/D.
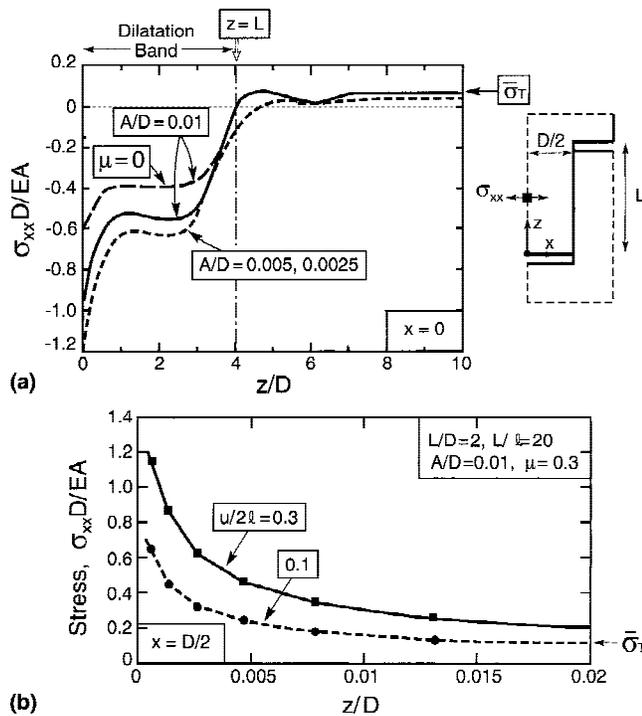
FIG. 9. (a) Transverse stresses for several interface conditions. Note that the compression within the bands is not constant. (b) Concentrated tensile stresses that exist at the extremity of the dilatation band.

sufficient tensile stretch to hold the system together. The interlayer between the plate edges must be weak enough to separate before the plates fail, to ensure that multiple dilatation bands form. Along the slipping interfaces, the organic mediates the internal friction, acting as a solid lubricant.

V. CONCLUSION

This study has identified four design principles that underlie the robustness of nacre. (i) The brittle phase has a tabular morphology with plate size, aspect ratio, and topological arrangement chosen to maximize the inelastic strain. (ii) The amplitudes and wavelengths of the nanoscale asperities on the plate surfaces provide strain hardening large enough to ensure formation of multiple dilatation bands but not so large that the plates fracture internally. (iii) The polymer interlayer has sufficient adherence and transverse stretch that the plates remain intact in the regions between the dilatation bands, where transverse tensile strains are generated. (iv) The same polymer interlayer appears to provide enough lubrication that interface slip is frictionless.

REFERENCES

1. J.D. Currey, Proc. R. Soc. London, Ser. B **196,** 443 (1977).
2. J.D. Currey, in *The Mechanical Properties of Biological Materials,* edited by J.F.V. Vincent and J.D. Currey (Symposia of the Society for Experimental Biology **34,** Cambridge Univ. Press, Cambridge, United Kingdom, 1980), p. 75.
3. A.P. Jackson, J.F.V. Vincent, and R.M. Turner, Proc. R. Soc. London, Ser. B **234,** 415 (1988).
4. H. Kessler, R. Ballarini, R.L. Mullen, L.T. Kuhn, and A.H. Heuer, Comput. Mater. Sci. **5,** 157 (1996).
5. A.P. Jackson, J.F.V. Vincent, and R.M. Turner, J. Mater. Sci. **25,** 3173 (1990).
6. B.L. Smith, T.E. Schaffer, M. Viani, J.B. Thompson, N.A. Frederick, J. Kindt, A. Belcher, G.D. Stucky, D.E. Morse, and P.K. Hansma, Nature **399,** 761 (1999).
7. S. Kamat, X. Su, R. Ballarini, and A.H. Heuer, Nature **405,** 1036 (2000).
8. R.Z. Wang, Z. Suo, I.A. Aksay, and A.G. Evans (submitted for publication).
9. K.E. Gunnison, M. Sarikaya, J. Liu, and I.A. Aksay, in *Hierarchically Structured Materials,* edited by I.A. Aksay, M. Sarikaya, and D.A. Tirrell (Mater. Res. Soc. Symp. Proc. **255,** Pittsburgh, PA, 1992), p. 171.
10. L. Addadi, S. Weiner, Angew. Chem., Int. Ed. Engl. **31,** 153 (1992).
11. A.G. Evans, Philos. Trans. R. Soc. London, Ser. A **315,** 511 (1995).
12. C.G. Levi, J.Y. Yang, B.J. Dalgleish, F.W. Zok, and A.G. Evans, J. Am. Ceram. Soc. **81,** 2077 (1998).
13. J.C. McNulty, F.W. Zok, G.M. Genin, and A.G. Evans, J. Am. Ceram. Soc. **82,** 1217 (1999).
14. J.B. Davis, D.B. Marshall, and P.E.D. Morgan, J. Eur. Ceram. Soc. **20,** 583 (2000).
15. M.S. Hu and A.G. Evans, Acta Metall. **37,** 917 (1989).
16. M.D. Thouless, Thin Solid Films **181,** 397 (1989).
17. M.D. Thouless, J. Am. Ceram. Soc. **73,** 2144 (1990).
18. T. Bai, D.D. Pollard, and H. Gao, Nature **403,** 753 (2000).
19. M.Y. He and J.W. Hutchinson, Int. J. Solids Struct. **25,** 1053 (1989).
20. J.W. Rudnicki and J.R. Rice, J. Mech. Phys. Solids **23,** 371 (1975).
21. J.W. Hutchinson and V. Tvergaard, Int. J. Solids Struct. **17,** 451 (1981).
22. W.W. Tworzydlo, W. Cecot, J.T. Oden, and C.H. Yew, Wear **220,** 113 (1998).
23. I.A. Polonky and L.M. Keer, Wear **231,** 206 (1999).
24. A.G. Evans, Acta Mater. **45,** 23 (1997).

APPENDIX I: IMPORTANCE OF DUCTILITY FOR ROBUST MECHANICAL PERFORMANCE

There is an appreciable literature on the connection between the inelastic strain capacity of a material and its mechanical robustness. The key issue is that the structural performance of a material is ultimately dominated by its ability to redistribute stress at strain concentration sites (imperfections, corners, holes, etc.), to eliminate stress concentrations.[24] This requires that the material be inelastic, with a strain capacity appreciably in excess of the elastic strains. Otherwise, materials are susceptible to unpredictable failures from imperfections.

The underlying principle is as follows. The material around imperfections responds to external loads in a manner governed largely by displacements, whereupon

inelastic strains reduce stress concentrations.[13,25] In the limit, the inelastic strains are large enough to completely eliminate the stress concentration. The behavior is exemplified by the notch response. Materials that exhibit net-section strength undiminished by the notch are those used in practical load bearing structures. An illustration for a material comprising a continuous lanthanum phosphate host phase, embedding a woven framework of mullite in two orthogonal orientations, is shown on Fig. A1.[14] These results and others have demonstrated that inelastic strains greater than about 4 times the elastic strain are sufficient to impart notch insensitivity.

As in the case of nacre, the response of the fibrous oxide in shear is softer than in tension along the reinforcement directions (Fig. A1) and the compressive stress/strain response is linear.
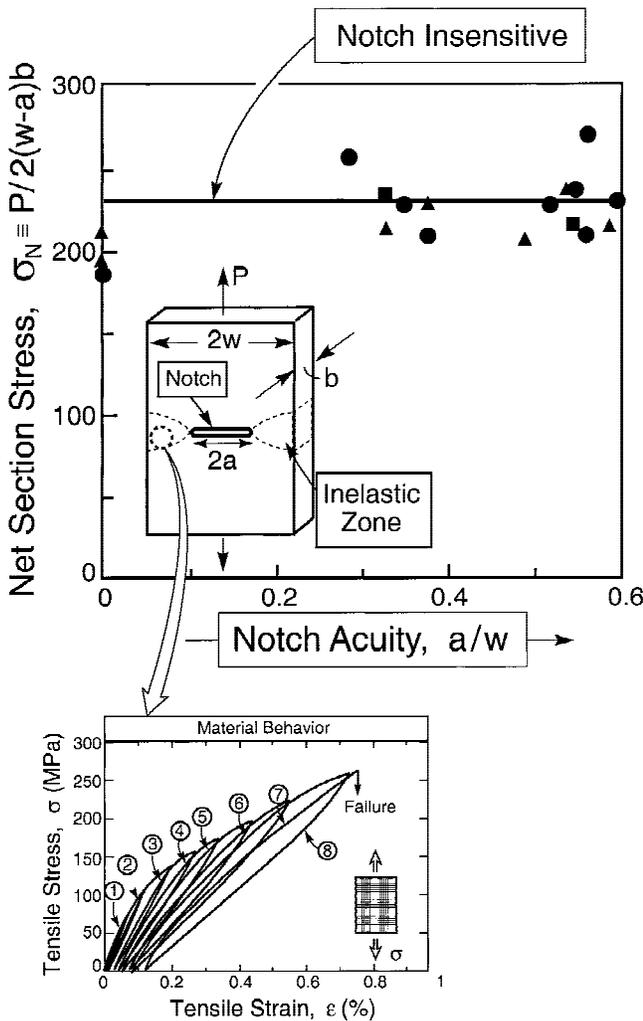

FIG. A1. "Notch insensitive" behavior measured for a material comprising a fibrous mullite framework in a lanthanum phosphate matrix. The inset shows the corresponding inelastic strains measured in tension on an unnotched coupon.[14]

APPENDIX II: ANALYTICAL MODEL

An analytical model for the slip response assumes that the asperities remain rigid (zero elastic compression). Then, the behavior can be simulated by imagining a wedge of material inserted at the interface, equal in thickness to the rigid body displacement caused by slip. This thickness, δ, is given by

$$\delta = A \sin[(\pi/2)u/l] \quad . \tag{B1}$$

The transverse compressions in the band induced by slip are

$$\epsilon_c = \delta/D \quad ,$$

$$\sigma_c = E\epsilon_c = \sigma_{ss} \sin[(\pi/2)u/l] \quad ,$$

$$\sigma_{ss} = EA/D \quad . \tag{B2a}$$

These stresses are partially offset by a Poisson contraction induced by the pull-out stress. The modified compression is

$$\sigma_c = \sigma_{ss} \sin[(\pi/2)u/l] - \nu\sigma \quad . \tag{B2b}$$

The result is approximate since the axial stress in the pull-out zone is nonuniform, as elaborated in the text. Assuming Coulomb friction, the average shear stress is related to the normal stress by

$$\tau = \mu\sigma_c \quad . \tag{B3}$$

Force equilibrium within the band requires that the bridges stress be related to the shear stress by

$$\sigma = \tau[L - u]/D \quad . \tag{B4}$$

Combining Eq. (B4) with Eqs. (B1) and (B2) gives

$$\sigma D^2/EAL = \mu(1 - u/L) \sin[\pi\Delta]/[1 + \mu\nu(L/D) \\ (1 - u/L)] \quad . \tag{B5a}$$

In terms of the key nondimensional parameters and for the displacements of present interest, $u \ll L$, Eq. (B5a) becomes

$$\Sigma = 2\mu \sin(\pi\Delta)/[1 + \mu\nu L/D] \quad . \tag{B5b}$$

Accordingly, the stress/strain relation (for $u \ll L$) becomes

$$\epsilon_p \approx (2l/\pi S) \sin^{-1}\{\Sigma(1 + \mu\nu L/D)/2\mu\} \quad . \tag{B6}$$

The deviations of the numerical results from this simple analytical result provide some useful insights. There appear to be three principal effects: (i) As the asperity amplitude *A/D* decreases from 0.001 to 0.005, the nondimensional peak stress *decreases* by about 20% but remains constant as *A/D* is further reduced (Fig. 6). (ii) The peak occurs at a displacement *smaller* than that expected from Eq. (B1). That is, the maximum arises at $\Delta < 0.5$,

before the asperities juxtapose (Figs. 6 and 7). (iii) At zero friction coefficient, there is still a finite resolved force in the pull-out direction. These deviations are attributable to the combined influences of the elastic deformations and the normal tractions, σ_N [Fig. 3(c)]. One elasticity effect is the compression of the juxtaposed asperities. This compression reduces the stress maximum, accounting primarily for the extra influence of A/D. A second elasticity effect is responsible for the greater effect of L/D on the stresses than that attributable to the Poisson contraction. It suggests an influence of the elastic stretching of the plate in the pull-out region on the sequencing of the asperity motions. Finally, at small μ, deviations arise because the geometric simplification neglects the effect of the *normal tractions,* σ_N, that still contribute, even when $\mu = 0$ [Fig. 3(c)].